ACS APPLIED MATERIALS & INTERFACES

Research Article

www.acsami.org

Directed Liquid Phase Assembly of Highly Ordered Metallic Nanoparticle Arrays

Yueying Wu,[†] Nanyi Dong,[‡] Shaofang Fu,[†] Jason D. Fowlkes,[§] Lou Kondic,[‡] Maria A. Vincenti,[∥] Domenico de Ceglia,[∥] and Philip D. Rack[†,§,*]

[†]Department of Materials Science and Engineering, The University of Tennessee, Knoxville, Tennessee 37996, United States

[‡]Department of Mathematical Sciences, New Jersey Institute of Technology, Newark, New Jersey 07102, United States

[§]Center for Nanophase Materials Sciences, Oak Ridge National Laboratory, Oak Ridge, Tennessee 37381, United States

[∥]Charles M. Bowden Research Laboratory, National Research Council−AMRDEC, Redstone Arsenal, Huntsville, Alabama 35898, United States

Supporting Information

ABSTRACT: Directed assembly of nanomaterials is a promising route for the synthesis of nanoscale materials. In this paper, we demonstrate the directed-assembly of highly ordered two-dimensional arrays of hierarchical nanostructures with tunable size, spacing and composition. The directed assembly is achieved on lithographically patterned metal films that are subsequently pulse-laser melted; during the brief liquid lifetime, the pattened nanostructures assemble into highly ordered primary and secondary nanoparticles, with sizes below that which was originally patterned. Complementary fluid-dynamics simulations emulate the resultant patterns and show how the competition of capillary forces and liquid metal−solid substrate interaction potential drives the directed assembly. As an example of the enhanced functionality, a full-wave electromagnetic analysis has been performed to identify the nature of the supported plasmonic resonances.

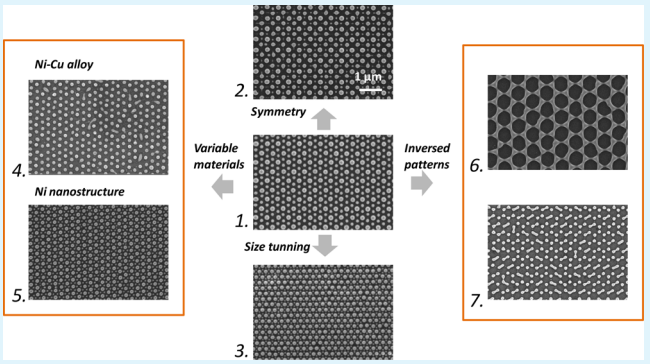

KEYWORDS: *nanoparticle array, directed assembly, dewetting, laser, plasmonics*

INTRODUCTION

Directed assembly of nanomaterials is a promising route for the synthesis of advanced materials and devices. To this end, several groups have demonstrated interesting nanoparticle arrays through the self-assembly of metallic thin films via solid state or liquid phase dewetting at elevated temperatures. Nanoparticles with a correlated size and spacing result from two-dimensional (2D) thin film instabilities[1−8] and pseudo 1-dimensional (1D) Rayleigh−Plateau instabilities.[9−15] The assembly of nanoparticles from thin film dewetting has the advantage of simplicity, high throughput and low cost. Several studies have shown functional properties from self- and directed assembly of metallic nanoparticles via solid and liquid phase dewetting, for example, plasmonics,[16−18] modified surface optical properties,[19] magnetic nanoparticles,[18,20] catalyst for nanowire growth[21,22] and as a catalyst for metal assisted chemical etching of high-aspect-ratio silicon nanowires.[23] However, highly ordered arrays of metallic nanoparticles with precise size and position are desired for enhanced functionality. In terms of a 2D nanoscale ordering, topographically patterned substrates or patterned polymers have been used to control individual nanoparticles as well as ordered nanostructures.[24−31] Ye et al. have recently demonstrated directed assembly of nickel nanostructures by varying the orientation of single crystal films coupled with oriented thin film patterns grown on MgO.[5] Well-aligned stripe patterns of gold and silver nanoparticles at micrometer scales were achieved by dewetting a floating film of nanoparticles on a water surface.[32] Meanwhile, the liquid phase assembly of nanoparticles from lithographically patterned lines and rings has also been studied and a correlated length scale results from a modified Rayleigh−Plateau instability of pseudo 1D filaments deposited on a substrate. Precise nanoparticle size and spacing were demonstrated by imposing "synthetic" sinusoidal[9] or square-wave surface perturbations[33] on the filament surface. The perturbations with amplitudes >10 nm and fast growth rates dominate the filament breakup, translating into highly ordered nanoparticles with well-defined spacing and size.

In spite of the significant advances that have been made in nanoparticle patterning/organization, demands still remain to assemble patterns with multiple size particles and variable compositions in a fast, effective way. In this paper, we

Received: January 31, 2014
Accepted: April 1, 2014
Published: April 1, 2014

demonstrate a new strategy for ordering 2D complex and hierarchical nanostructures with tunable primary and secondary nanoparticles. Most notably, we will demonstrate the formation of a multilength scale nanoparticle network with controllable size, symmetry and composition using a single lithography step. Complementary hydrodynamic numerical simulations of the fluid dynamics emulate the resultant pattern evolution and provide insight into the complex directed assembly dynamics. The capillary force induced by the lithographically patterned architecture coupled with the long-range interfacial forces act in concert at the nanoscale to order the final hierarchical nanoparticle ensemble.

EXPERIMENTS AND RESULTS

The simple process flow and initial patterned morphology is illustrated in Figure 1. The top-down and tilted view of the initial lithography step is shown in Figure 1a,b, respectively. The generated pattern is an array of metal cylinders (yellow) in this case with a hexagonal close packed geometry: D is the cylinder diameter; α is the symmetry angle (60°); S is center-to-center spacing (or pitch) of two nearest neighbor cylinders. Next, the patterned cylinders are (c) coated (green) with a continuous metal layer referred to here as the covering film.

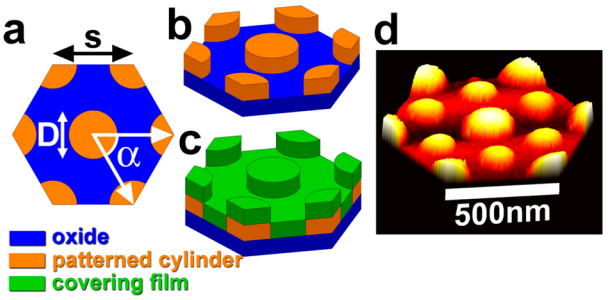

Figure 1. Schematic illustrating the simple patterning process of the hexagonal close packed symmetry used as the template for the liquid phase directed assembly process. The first step (a) and (b) involves patterning cylinder arrays with a specific thickness, diameter D and center-to-center spacing S (yellow). The second step (c) is to cover the cylinders with a continuous thin film (green). Panel d is an atomic force microscope image of a resultant interpenetrating primary and secondary particle array.

The patterned samples are irradiated with an 18 ns, 248 nm KrF excimer laser at sufficient fluence to melt both the cylinder and intercylinder or interstitial regions. Figure 1d illustrates an atomic force microscopy image of a resulting directly assembled nanoparticle unit cell, showing the ordered primary and secondary particles. As will be shown, regimes exist in which the initial patterned cylinders impose topographical variation along the thin film and act as so-called "synthetic perturbations", which directs the liquid phase assembly and leads to perfectly ordered primary and secondary particles. The cylinder geometry, spacing, thickness and diameter as well as the covering film thickness can all be varied independently to tune the size and spacing of the primary and secondary interpenetrating nanoparticle lattices. Notably, two materials can be used as the cylinder pattern and covering layer, thus alloy nanoparticles can be synthesized and tuned conveniently by varying the ratio of cylinder thickness to covering layer thickness. Obvious limitations of the process are 1) the underlying substrate must have a higher melting temperature than the patterned material, 2) the optical/thermal properties of the assembled materials must be compatible with coupling to a pulsed laser adequate for melting, 3) and the final wetting angle of the assembled nanoparticles is dictated by the balance of the surface tensions of the solid–air, liquid–substrate and liquid–air. While this precludes some compound materials, it is envisioned that elemental or alloyed nanoparticles can be synthesized and then postannealed in various ambients to form complex compound materials.

Initially, we demonstrate the specific case in which both the cylinder array and covering film materials are both copper and both 9 nm thick. Copper is selected because it is abundantly used in electronic applications and as a noble metal it is attractive for plasmonic-based applications. In the first series of experiments, cylinders with D = ~350 nm were patterned in a hexagonal-close-packed geometry with a variable S ranging from 400 to 700 nm (see Table 1 for specific pattern parameters). Figure 2a,b shows scanning electron microscope (SEM) images of an as-synthesized pattern for the 500 nm S before and after laser irradiation. Figures 2c–f are high-resolution micrographs illustrating the resultant nanoparticle arrays (note Figure 2d is a high-resolution image of 2b). Spatial correlation functions (SCF) of the resultant nanoparticle networks (see the Supporting Information) reveal both short-

Table 1. Synthesis Parameters (Cylinder Thickness, Covering Layer Thickness, Cylinder Diameter (D), Cylinder Center-to-Center Spacing (S)) for each SEM Image Presented in Figures 2 and 4[a]

figure	cylinder thickness, nm	cover layer thickness, nm	diameter (D), nm	spacing (S), nm	D (primary), nm	D (secondary), nm	note
2a,b,d	9	9	360	400	220	64	Cu
2c	9	9	350	500	215	120	Cu
2e	9	9	340	600	215	185	Cu
2d,f	9	9	340	700	215	178	Cu
4a	9	9	350	500	215	120	Cu
4b*	9	9	350	500	215	170	square lattice
4c	20	9	350	500	240	130	Cu
4d	9	9	230	300	162	66	Cu
4e	9	9	350	500	145	132	Cu–Ni
4f	9	9	360	400	190	50	Ni
4g	9	15	140	900	N/A	N/A	inverted mesh
4h	9	15	140	900	N/A	265	inverted array

[a]All cylinder symmetries were hexagonal except as denoted by an asterisk, which had a square lattice. The primary and secondary particle diameters are also included.

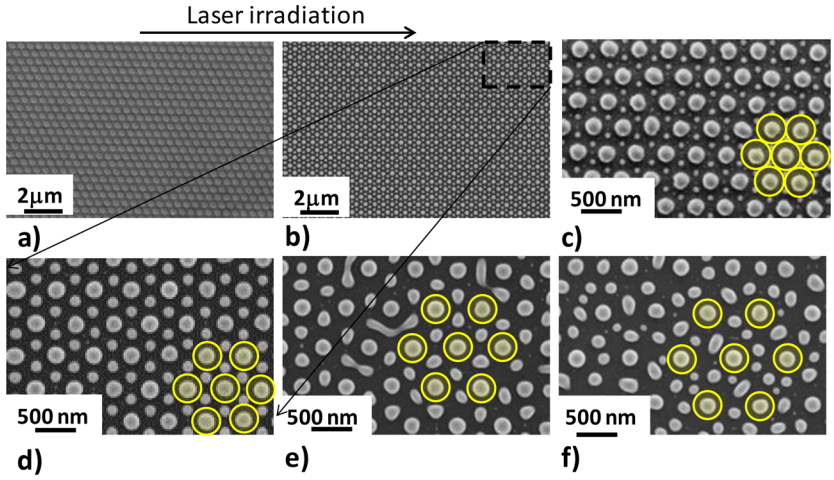

Figure 2. (a) Scanning electron micrographs of an as-synthesized array of hexagonal close packed copper cylinders 9 nm thick and D = 350 nm, S = 500 nm and covered with a 9 nm thick copper film. (b) Liquid phase assembly of primary and secondary nanoparticles induced by pulsed laser exposure. Higher magnification scanning electron micrographs of resultant nanoparticles with a common D = 350 nm and variable S illustrating the ability to independently control the primary and secondary particle size. Cylinder S: (c) 400 nm, (b) and (d) 500 nm, (e) 600 nm and (f) 700 nm. The transparent circles illustrate the location and approximate diameter of the original cylinders.

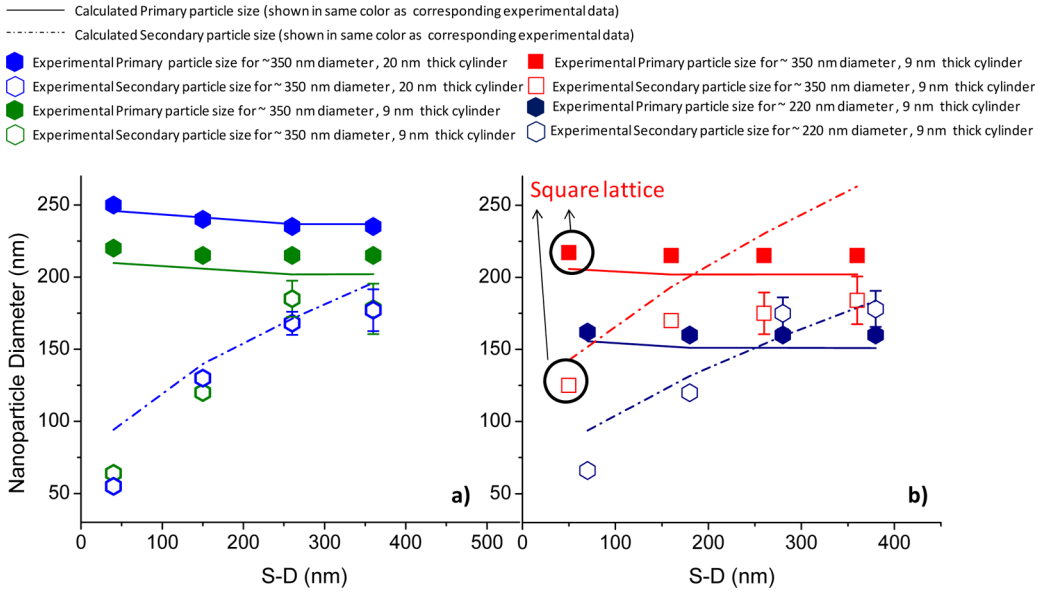

Figure 3. Plots of experimental and calculated primary and secondary particle sizes versus patterned distances between cylinders ($S - D$). (a) Particle sizes for hexagon lattices with D = ~350 nm, two cylinder thicknesses (blue, 9 nm; green, 20 nm) and 9 nm covering layer. (b) Particle sizes for hexagon lattice (dark blue) with D = ~220 nm, 9 nm cylinder thickness and 9 nm covering layer; particle sizes for square lattice (red) with D = ~350 nm, 9 nm cylinder thickness and 9 nm covering layer. The plots illustrate that the patterned cylinder volume controls the primary particle size and the interstitial volume controls the secondary particle size (here ($S - D$) was chosen as x-axis to better present interstitial dimension that correlates to secondary particle size); thus, independent control of the primary and secondary lattices can be directly assembled with a careful consideration of the original patterned parameters. Solid lines are the estimated volumes of the primary particles, dashed lines are estimated volumes of the secondary particles, the symbol shapes denote the type of lattice cylinders are arranged in (hexagonal or square), filled symbols are primary particle sizes and unfilled symbols are secondary particle sizes and the different colors represent different thin film dimensions.

and long-range ordering from the original patterns as well as the secondary particles. Interestingly, as S increases, the primary particles remained ordered; however, competing fluid instabilities, as discussed below, degraded the secondary particle order. Estimations of the time−temperature profiles of a 9 and 18 nm thick film for a single laser pulse (140 mJ/cm^2) confirm that the incident laser fluence is sufficient to melt both the 18 nm cylinder and 9 nm intercylinder or "interstitial" regions and the liquid lifetimes are ~15 ns. The simulations also suggest that a lateral thermal gradient also exists between the, hotter, thicker cylindrical regions (18 nm) and the cooler, interstitial film (9 nm); thus, second-order thermocapillary effects could also be operative and we plan to consider them in future work.

As demonstrated in Figure 2, primary nanoparticles form in spatial phase with the lithographically patterned cylinders; additionally, a secondary interpenetrating lattice of nanoparticles evolves associated with the interstitial film. Figure 3a includes a plot of the measured primary and secondary nanoparticle diameter (green markers) for the patterns shown in Figure 2. Also included in Figure 3 are plots of calculated

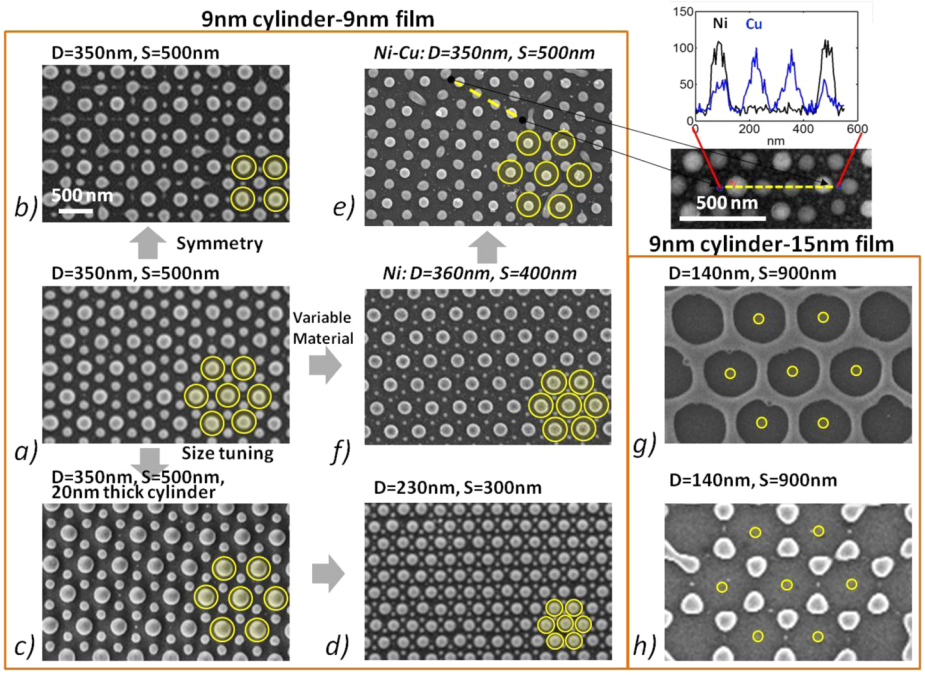

Figure 4. Collage of nanoparticle arrays that have been directly assembled with variable synthesis parameters (see Table 1). On the basis of arrays with initial dimension D = 350 nm, S = 500 nm (a), it demonstrates the ability to control symmetry (b), particle sizes (c and d), composition (e, integrated Cu−Ni alloy nanoparticles; f, Pure Ni nanoparticles) and to achieve inverted nanostructures (g and h). The top-right inset for image e illustrates an energy dispersive X-ray spectroscopy line scan showing Cu−Ni alloy primary particles and pure Cu secondary particles made from patterned Ni cylinders and Cu covering layer (the yellow dashed line illustrates the direction and length of the line scan, from a similar direction but not exact same area as shown in e. Image g illustrates an example where the symmetry inverts as mass flows away from the original patterned cylinder area and assembles a continuous "mesh" structure and (h) an inverted nanoparticle array resulting from a longer liquid lifetime relative to structure (g). See Table 1 for specific parameters. Images a−h are at the same magnification. The yellow transparent circles illustrate the location and approximate diameter of the original cylinders.

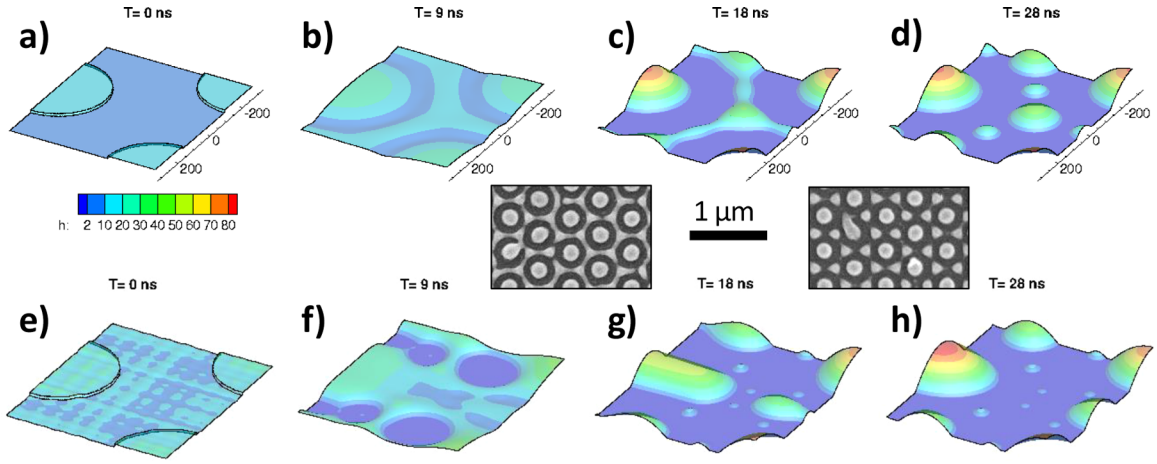

Figure 5. Hydrodynamic simulations illustrating the temporal evolution of a 350 nm diameter cylinder with S = 600 nm. Sequences a−d) and e−h illustrate the evolution without and with the inclusion of random perturbations of 0.5 nm maximum amplitude, respectively. Insets show SEM images for D = 350 nm and S = 500 nm at early stages of the liquid phase assembly process, that agrees well with the computed evolution.

primary and secondary particle diameters (assuming a wetting angle of 79°) calculated from (1) the cylinder volume and (2) the interstitial volume (see the Supporting Information for details) for a series of patterns with varied dimensions, which highlights the ability to finely tune nanoparticle size via the directed assembly process. Comparing the calculated and measured particle sizes confirms that primary particles are derived mostly from mass located in the thicker, cylindrical regions while the secondary particles derive their mass from the interstitial regions. A more careful observation shows that the primary particle sizes are slightly larger than the calculated sizes, while the secondary particle sizes are smaller. This is reasonable considering the mass flow directed by initial boundary perturbation. As shown in the hydrodynamic simulation (Figure 5), the perturbation leads to film rupture at a certain point just beyond the patterned cylinder, hence some material in the "interstitial" area flows into the primary nanoparticles; the small amount of material only slightly affects the larger primary particles and more significantly modifies the mass of the secondary particles. For patterns with larger spacing,

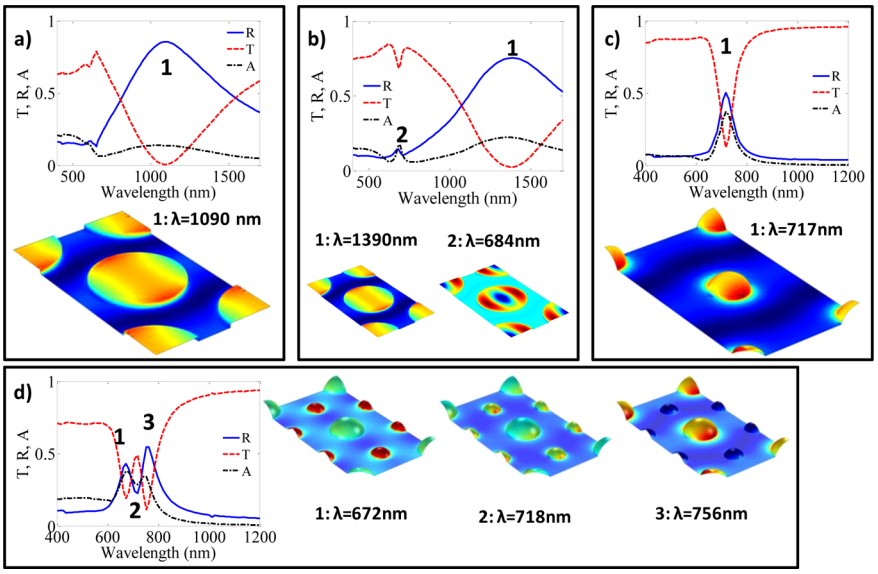

Figure 6. Simulated transmission, reflection and absorption spectra and magnetic field amplitude at specific wavelengths for (a) 18 nm and (b) 9 nm D = 350 nm and S = 500 nm cylinder arrays; (c) hemispherical nanoparticles in a hexagonal array mimicking the lone primary particle array; (d) directly assembled hemispherical primary and secondary nanoparticle array. The patterned cylinders with 18 nm thickness exhibit a single broadband plasmonic resonance. A similar field localization is found for higher wavelength when reducing the height of the nanodisks to h = 9 nm. In this second scenario, a higher order resonance is also visible at shorter wavelengths. A narrow-band resonant feature characterizes primary nanoparticles. Two distinct field localizations can be found for the array composed of primary and secondary nanoparticles, i.e., when the resonance of one or the other nanoparticle is excited. However, for an intermediate wavelength between the two resonances, the magnetic field is localized on all nanoparticles, revealing the interaction between the two resonant features.

particularly the square lattice shown in Figure 4b, which have a larger interstitial area relative to the hexagon lattice with same initial dimensions, the average secondary nanoparticle size are clearly smaller than the calculated size. Additionally, as the particle size increases, the standard deviation of secondary particles' size increases due to the pattern degradation that is attributed to the spinodal instability of a thin fluid film, discussed in more detail in the hydrodynamic simulation shown in Figure 5. Figure 4 is a collage of SEM images of assembled nanoparticle arrays synthesized with different parameters, which demonstrates that, relative to a, the (b) geometry/symmetry, (c) and (d) primary and secondary particle size and (e) and (f) particle composition can all be varied independently (see Table 1 for pattern parameters). Specifically, the interpenetrating Cu−Cu/Ni nanoparticle lattice synthesized with a nickel cylinders covered with a copper covering layer is demonstrated in Figure 4e (note EDX line scan that shows different composition of primary and secondary nanoparticles). Such hybrid nanoparticle arrays may inspire emergent and multiple functionalities.[12,18,34−36] Figure 4g, h illustrate an interesting observation for a different cylinder/covering layer thickness combination in which the hydrodynamics invert the original pattern. We suspect that this is due to thermocapillary effects and warrant further study. The measured and predicted primary and secondary particle sizes for Figure 4a−f are also included in Figure 3.

To understand the directed assembly evolution, simulations based on fluid mechanical modeling were performed. The simulations are based on the long-wave (lubrication) model that includes capillary forces as well as the fluid−solid interaction;[37] more details are given in the Methods section. Figure 5a−d shows a sequence of images resulting from simulations for cylinders 9 nm thick, D = 350 nm, S = 600 nm and again covered with a uniform 9 nm thick film. For efficiency, we simulate only a small fraction of the experimental domain, which is, however, large enough to illustrate the instability mechanism. The initial pattern induces curvatures both in-plane and out-of-plane (height or z-dimension) and thus once melted, capillary forces cause material to evolve, producing a radial undulation around each cylinder. The interfacial potential mentioned above causes the minimum in the undulation to advance toward the substrate and eventually leads to the circular ring around the original cylinders, effectively separating the cylinder region from the rest of the film. Each cylinder then forms a drop in order to minimize its surface area. Therefore, each cylinder forms a primary particle, while the interstitial film area leads to the formation of a filament that eventually breaks up. The two SEM images, shown as insets in Figure 5, capture the earlier stages of the directed assembly process and suggest that these earlier stages are consistent with the progression demonstrated by the simulations. Overall, the simulations capture not only the spatial evolution but also the overall time scale of evolution, as suggested by the simulated liquid lifetimes.

Figure 2 shows that, for a small S, the secondary particles are highly ordered, whereas for larger S (>∼600 nm for the D = 350 nm), the secondary particle ordering degrades. This finding can be understood by considering the so-called spinodal instability of a thin fluid film exposed to fluid−solid interaction forces (see reference 37 and references therein, as well as the Supporting Information). Essentially, small height perturbations in a nominally uniform film may be unstable, and, given enough time, can lead to instability. To illustrate this process, Figure 5e−h shows results of the simulations where, in addition to the cylinder geometry considered so far, we include random perturbations of maximum amplitude of 0.5 nm. These additional simulations break the originally imposed symmetry and, in the case considered in Figure 5, lead to formation of

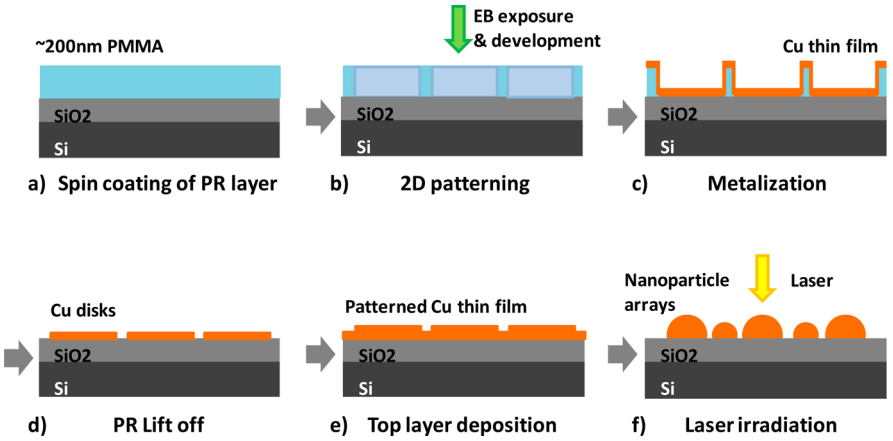

Figure 7. Process flow of directed assembly of highly ordered Cu nanoparticle arrays.

more disordered patterns. Additional simulations for cylinders that are more closely spaced (results not given for brevity) show that, in such a geometry, random perturbations do not play a role because they do not have time to grow and influence the formation of secondary particles. The Supporting Information shows animations obtained by hydrodynamic simulations.

OPTICAL SIMULATION OF NANOPARTICLE ARRAYS

Finally, as an example of the enhanced functionality of the hierarchical nanoparticle array formed by the liquid phase directed assembled, a full-wave electromagnetic analysis of several representative periodic arrays has been performed to identify the nature of the plasmonic resonances supported by originally patterned cylinders, laser self-assembled cylinders (no-covering layer) and directly assembled primary and secondary particles. It is well-known that surface plasmons are highly sensitive to factors such as geometry, size, shape and the surrounding medium.[38−42] The comparison between the three different patterns provides an insight of the advantage in potential optical application related to the directed assembled nanoparticles. Specifically, we simulated patterned 9 and 18 nm cylinders (no bridging continuous film), assembled hemispherical nanoparticles from laser treated 9 nm cylinders, which have a diameter of 170 nm and finally the ordered primary and secondary hemispherical nanoparticles from the directed assembly process illustrated in Figure 2d. To be consistent, all the patterns have S = 500 nm. We evaluated transmission (T), reflection (R) and absorption (A) spectra as described in the Methods section. Figure 6a, b illustrates that the D = ~350 nm patterned cylinders exhibit a broadband plasmonic resonance for an input wavelength of approximately λ = 1100 nm that red-shifts when the height of the cylinders decreases from h = 18 nm to h = 9 nm. Such red-shift is due to the increase of the effective refractive index of the Hankel-type surface plasmon polariton (SPP) propagating in the cylinder.[43,44] A higher order resonance is also visible at shorter wavelengths for the array with h = 9 nm cylinders (Figure 6b). Moreover, a blue-shift of the resonances is expected when the radius of the cylinder is reduced. Because of their aspect ratio, the cylinders can be treated as oblate spheroids with a large depolarization factor along the revolution axis and they behave like circular patch nanoantennas.[44]

A different scenario is associated with the array of laser treated samples that evolve into hemispherical nanoparticles or nanocaps. Here a narrow-band resonant feature appears around a wavelength of nearly 700 nm when the diameter of the caps is D = 170 nm (Figure 6c). The dipolar resonance of the nanoparticle blue- or red-shifts depending on the particle radius. For this reason, the directed assembly array composed of primary and secondary nanoparticles (Figure 6d), i.e., with D = 120 nm and D = 200 nm radii, exhibits two distinct resonances, at λ = 670 nm and λ = 760 nm. Because of the proximity between nanoparticles (the nearest neighbor distance is on the order of 300 nm), the two resonances interact producing broader spectral features that can be tailored to enhance absorption (or suppress transmission) in a desired spectral range. The narrow band resonance features generated in directed assembled interpenetrating nanoparticles could be attractive in many plasmonic-based applications.

CONCLUSION

In conclusion, we demonstrate that hierarchical nanoparticle arrays with controllable size, composition and symmetry can be realized via a convergence of top-down lithography and a bottom-up self-assembly approach. Importantly, the particle sizes realized can be smaller than the patterned lithographic geometry. The directed assembly has been rationalized using computational fluid dynamics and the order-to-disorder transition at larger S values are attributed to competing thin film instabilities caused by random perturbations. The hierarchical nanoparticle arrays demonstrate multimodal plasmonic resonances with narrower spectral widths relative to the originally lithographically patterned cylinder arrays.

METHODS

Pattern Synthesis. A detailed process flow is illustrated in Figure 7, which shows the step-by-step synthesis steps for the highly ordered Cu nanoparticle arrays. The copper cylinder patterns were lithographically patterned on silicon wafers coated with a 100 nm silicon dioxide via electron beam lithography using a positive tone resist. The resist was spin coated at 4000 rpm to ~200 nm thick (Figure 7a. The circular patterns were exposed to 1200 μC/cm^2 and developed in an IMBK:IPA (1:3) developer for 80 s (Figure 7b). The resist was lifted off in acetone with ultrasonic agitation after metallization (Figure 7c,d). Then the top metal was deposited and the sample was laser irradiated (Figure 7e,f). The copper cylinders and covering layer thin film were both DC sputter deposited using an AJA DC sputtering system equipped with 75 mm sputter targets. The DC power was 30

W and chamber pressure was set at 3 mTorr during sputtering. The sputtering rate was measured by both reflectometry and atomic force microscopy to be 0.16 nm/s. The arrays were exposed to 1−3 18 ns KrF excimer pulses at a fluence of 140 mJ/cm^2. Scanning electron microscopy and energy-dispersive X-ray spectroscopy was performed with a FEI Nova Lab 600 dual beam and an Auriga cross beam system. A Dimension 3100 atomic force microscope (AFM) was used to measure assembled nanoparticle arrays.

Hydrodynamic Simulations. The dynamics is described by applying a long wave (lubrication) approximation, which allows reducing the Navier−Stokes equations to a single differential equation for the fluid thickness.[45] Two assumptions were made: that the liquid metal behaves like a Newtonian fluid (see also references 1 and 29 in reference 45 regarding this point), and the pulsed laser irradiation leads to very rapid heating so that the evolution takes place in a liquid phase with fixed and uniform temperature. This approach leads to the following nonlinear fourth order partial differential equation[45]

$$3\mu\frac{\partial h}{\partial t} + \gamma\nabla\cdot(h^3\nabla\nabla^2 h) + \nabla\cdot[h^2\nabla\Pi(h)] = 0 \tag{1}$$

where h (x, y, t) is the film thickness, x and y are the in-plane coordinates, $\nabla = (\partial/\partial x,\partial/\partial x)$, μ is the dynamic viscosity and γ is the surface tension. Here, the second term corresponds to the capillary forces and the third term is due to liquid−solid interaction. The functional form of $\Pi(h)$ that has been applied in recent works[45] is of the form corresponding to an interface potential that includes competing long and short-range forces and has a minimum at nanoscale lengths[45]

$$\Pi(h) = \kappa f(h) = \kappa\left[\left(\frac{h_*}{h}\right)^n - \left(\frac{h_*}{h}\right)^m\right] \tag{2}$$

Here $\kappa = s/(Mh_*)$, where s is the spreading parameter, $m = 2$, $n = 3$ and $M = (n-m)/((m-1)(n-1))$. The spreading parameter can be related to the apparent contact angle θ via the Laplace Young condition $s = \gamma(1 - \cos\theta)$, here θ is chosen as $\theta = 79°$. h_* is the equilibrium film thickness. κ and h_* are related to the Hamaker constant A as $\kappa h_*^3 = A/6$.[45] Here, we use $h_* = 1$ nm, which is larger than the values expected for liquid metals, see ref 46, due to high computational cost involved in solving eq 1 in three spatial dimensions. The first term represents liquid solid repulsion whereas the second term stands for the attractive force, and both terms cancel out for a flat film of thickness h_*. Use of the lubrication approximation for the problem characterized by large contact angle and related accuracy issues were discussed in previous works.[45] The material parameters can be found in Table 1 in Wu et al.[10]

After using $\hat{h} = h/h_c$, $\hat{x} = x/x_c$, $\hat{y} = y/y_c$, $\hat{t} = t/t_c$ for nondimensionalization, eq 1 simplifies to the following:

$$\frac{\partial\hat{h}}{\partial\hat{t}} = -\nabla\cdot(\hat{h}^3\nabla\nabla^2\hat{h}) - K\nabla\cdot[\hat{h}^3 f'(\hat{h})\nabla\hat{h}] \tag{3}$$

Equation 3 is analyzed in the main body of the paper. Here

$$t_c = \frac{3\mu x_c^4}{\gamma h_c^3} \tag{4}$$

$$K = \frac{\kappa h_c^2}{3\mu h x_c^2}t_c = \frac{\kappa x_c^2}{\gamma h_c} \tag{5}$$

With the parameters chosen, and $x_c = h_c = 1$ nm, we find $t_c = 1.008 \times 10^{-11}$ s and $K = 1.608$.

Optical Modeling. The full-wave simulations have been performed by means of a finite element solver in the frequency domain (COMSOL Multiphysics, available at: http://www.comsol.com) to evaluate transmission, reflection and absorption spectra of a variety of synthesized arrays. An air superstrate and an SiO_2 substrate have been considered in all simulations. Optical data for Cu and SiO_2 have been taken from Palik's handbook.[47] Each array is illuminated by a linearly polarized plane wave (with electric field oriented along the nearest neighbor direction of the array) impinging at normal incidence from air. The simulation domain has been restricted to one rectangular unit cell by using Floquet boundary conditions on the boundaries perpendicular to the plane of the array (x−y plane) and perfectly matched layers to absorb radiation transmitted to the substrate and reflected back to the superstrate. Absorption has been calculated by integrating resistive losses in the Cu particles, i.e.,

$$A = \frac{1/2\omega\int_v \mathrm{Im}(\varepsilon_{Cu})|E|^2 d\nu}{I_{in}a_x a_y} \tag{6}$$

where ω is the angular frequency of the input plane wave, $\mathrm{Im}(\varepsilon_{Cu})$ is the imaginary part of the absolute permittivity of Cu, E is the electric field, I_{in} is the input irradiance and a_x and a_y are the periodicities along the x and y directions. Transmission is evaluated by integrating the z-component of the Poynting vector P_z on a plane Σ parallel to the array's plane in the far field region of the substrate, i.e., $T = (\int_S P_Z dS)/(I_{in}a_x a_y)$. Reflection is inferred as $R = 1 - T - A$.

■ ASSOCIATED CONTENT

Ⓢ Supporting Information

Analysis of the spatial ordering of nanoparticles, calculation of particle mass conservation, self-assembly of unpatterned Cu thin films and hydrodynamic simulation details. This material is available free of charge via the Internet at http://pubs.acs.org.

■ AUTHOR INFORMATION

Corresponding Author

*P. D. Rack. E-mail: prack@utk.edu. Tel.: 8659745344.

Notes

The authors declare no competing financial interest.

■ ACKNOWLEDGMENTS

Y. Wu and J. D. Fowlkes acknowledge support from the U.S. Department of Energy, Basic Energy Sciences, Materials Science and Engineering Division for sponsoring the aspects of this work related to understanding the fundamental mechanisms operative during liquid phase, thin film dewetting. P. D. Rack acknowledges support from NSF grant No. CBET-1235651. N. Dong and L. Kondic acknowledge support by NSF grant No. CBET-1235710. S. Fu acknowledges support from the TN-SCORE program funded by NSF EPS 1004083. M. A. Vincenti and D. de Ceglia acknowledge that their work was performed while holding a National Research Council Research Associateship awards at the U.S. Army Aviation and Missile Research Development and Engineering Center. A portion of this work related to the deposition of thin films and nanolithography was conducted at the Center for Nanophase Materials Sciences, which is sponsored at Oak Ridge National Laboratory by the Scientific User Facilities Division, Office of Basic Energy Sciences, U.S. Department of Energy.

■ REFERENCES

(1) Trice, J.; Thomas, D.; Favazza, C.; Sureshkumar, R.; Kalyanaraman, R. Pulsed-laser-induced Dewetting in Nanoscopic Metal films: Theory and Experiments. *Phys. Rev. B* **2007**, *75*, 235439.

(2) Krishna, H.; Shirato, N.; Yadavali, S.; Sachan, R.; Strader, J.; Kalyanaraman, R. Self-Organization of Nanoscale Multi layer Liquid Metal Films: Experiment and Theory. *ACS Nano* **2011**, *5*, 470−476.

(3) Henley, S. J.; Carey, J. D.; Silva, S. R. P. Pulsed-laser-induced Nanoscale Island Formation in Thin Metal-on-oxide Films. *Phys. Rev. B* **2005**, *72*, 195408.

(4) Palmer, J. S.; Swaminathan, P.; Babar, S.; Weaver, J. H. Solid-state Dewetting-mediated Aggregation of Nanoparticles. *Phys. Rev. B* **2008**, *77*, 195422.

(5) Ye, J.; Thompson, C. V. Templated Solid-State Dewetting to Controllably Produce Complex Patterns. *Adv. Mater.* **2011**, *23*, 1567−1571.
(6) Ye, J. P.; Thompson, C. V. Mechanisms of Complex Morphological Evolution During Solid-state Dewetting of Single-crystal Nickel Thin Films. *Appl. Phys. Lett.* **2010**, *97*, 071904.
(7) Herminghaus, S.; Jacobs, K.; Mecke, K.; Bischof, J.; Fery, A.; Ibn-Elhaj, M.; Schlagowski, S. Spinodal Dewetting in Liquid Crystal and Liquid Metal Films. *Science* **1998**, *282*, 916−919.
(8) Bischof, J.; Scherer, D.; Herminghaus, S.; Leiderer, P. Dewetting Modes of Thin Metallic Films: Nucleation of Holes and Spinodal Dewetting. *Phys. Rev. Lett.* **1996**, *77*, 1536−1539.
(9) Fowlkes, J. D.; Kondic, L.; Diez, J.; Wu, Y. Y.; Rack, P. D. Self-Assembly versus Directed Assembly of Nanoparticles via Pulsed Laser Induced Dewetting of Patterned Metal Films. *Nano Lett.* **2011**, *11*, 2478−2485.
(10) Wu, Y.; Fowlkes, J. D.; Roberts, N. A.; Diez, J.; Kondic, L.; González, A. G.; Rack, P. D. Competing Liquid Phase Instabilities during Pulsed Laser Induced Self-Assembly of Copper Rings into Ordered Nanoparticle Arrays on SiO_2. *Langmuir* **2011**, *27*, 13314−13323.
(11) Wu, Y. Y.; Fowlkes, J. D.; Rack, P. D.; Diez, J. A.; Kondic, L. On the Breakup of Patterned Nanoscale Copper Rings into Droplets via Pulsed-Laser-Induced Dewetting: Competing Liquid-Phase Instability and Transport Mechanisms. *Langmuir* **2010**, *26*, 11972−11979.
(12) Fowlkes, J. D.; Wu, Y. Y.; Rack, P. D. Directed Assembly of Bimetallic Nanoparticles by Pulsed-Laser-Induced Dewetting: A Unique Time and Length Scale Regime. *ACS Appl. Mater. Interfaces* **2010**, *2*, 2153−2161.
(13) Fuentes-Cabrera, M.; Rhodes, B. H.; Fowlkes, J. D.; Lopez-Benzanilla, A.; Terrones, H.; Simpson, M. L.; Rack, P. D. Molecular Dynamics Study of the Dewetting of Copper on Graphite and Graphene: Implications for Nanoscale Self-assembly. *Phys. Rev. E* **2011**, *83*, 041603.
(14) Lian, J.; Wang, L. M.; Sun, X. C.; Yu, Q. K.; Ewing, R. C. Patterning Metallic Nanostructures by Ion-beam-induced Dewetting and Rayleigh Instability. *Nano Lett.* **2006**, *6*, 2637−2637.
(15) Fowlkes, J.; Horton, S.; Fuentes-Cabrera, M.; Rack, P. D. Signatures of the Rayleigh-Plateau Instability Revealed by Imposing Synthetic Perturbations on Nanometer-Sized Liquid Metals on Substrates. *Angew. Chem., Int. Ed.* **2012**, *51*, 8768−8772.
(16) Lin, C. H.; Jiang, L.; Zhou, J.; Xiao, H.; Chen, S. J.; Tsai, H. L. Laser-treated Substrate with Nanoparticles for Surface-enhanced Raman Scattering. *Opt. Lett.* **2010**, *35*, 941−943.
(17) Wu, Y.; Fowlkes, J. D.; Rack, P. D. The Optical Properties of Cu-Ni Nanoparticles Produced via Pulsed Laser Dewetting of Ultrathin Films: The Effect of Nanoparticle Size and Composition on the Plasmon Response. *J. Mater. Res.* **2011**, *26*, 277−287.
(18) Sachan, R.; Ramos, V.; Malasi, A.; Yadavali, S.; Bartley, B.; Garcia, H.; Duscher, G.; Kalyanaraman, R. Oxidation-Resistant Silver Nanostructures for Ultrastable Plasmonic Applications. *Adv. Mater.* **2013**, *25*, 2045−2050.
(19) Reinhardt, H.; Kim, H. C.; Pietzonka, C.; Kruempelmann, J.; Harbrecht, B.; Roling, B.; Hampp, N. Self-Organization of Multifunctional Surfaces - The Fingerprints of Light on a Complex System. *Adv. Mater.* **2013**, *25*, 3313−3318.
(20) Krishna, H.; Gangopadhyay, A. K.; Strader, J.; Kalyanaraman, R. Nanosecond Laser-induced Synthesis of Nanoparticles with Tailorable Magnetic Anisotropy. *J. Magn. Magn. Mater.* **2011**, *323*, 356−362.
(21) Choi, W. K.; Liew, T. H.; Chew, H. G.; Zheng, F.; Thompson, C. V.; Wang, Y.; Hong, M. H.; Wang, X. D.; Li, L.; Yun, J. A Combined Top-down and Bottom-up Approach for Precise Placement of Metal Nanoparticles on Silicon. *Small* **2008**, *4*, 393−393.
(22) Guan, Y. F.; Pearce, R. C.; Melechko, A. V.; Hensley, D. K.; Simpson, M. L.; Rack, P. D. Pulsed Laser Dewetting of Nickel Catalyst for Carbon Nanofiber Growth. *Nanotechnol.* **2008**, *19*, 235604.
(23) Lianto, P.; Yu, S. H.; Wu, J. X.; Thompson, C. V.; Choi, W. K. Vertical Etching with Isolated Catalysts in Metal-assisted Chemical Etching of Silicon. *Nanoscale* **2012**, *4*, 7532−7539.
(24) Lopes, W. A.; Jaeger, H. M. Hierarchical Self-assembly of Metal Nanostructures on Diblock Copolymer Scaffolds. *Nature* **2001**, *414*, 735−738.
(25) Chen, X. C.; Li, H. M.; Fang, F.; Wu, Y. W.; Wang, M.; Ma, G. B.; Ma, Y. Q.; Shu, D. J.; Peng, R. W. Confinement-Induced Ordering in Dewetting and Phase Separation of Polymer Blend Films. *Adv. Mater.* **2012**, *24*, 2637−2641.
(26) Mukherjee, R.; Bandyopadhyay, D.; Sharma, A. Control of Morphology in Pattern Directed Dewetting of Thin Polymer Films. *Soft Matter* **2008**, *4*, 2086−2097.
(27) Moungthai, S.; Pham, T. C. H.; Rajaendran, A. A.; Stein, G. E. Ordered Arrays of Polymer Droplets with Triangular, Circular, and Rod-like Shapes. *Soft Matter* **2012**, *8*, 10026−10031.
(28) Harkema, S.; Schaffer, E.; Morariu, M. D.; Steiner, U. Pattern Replication by Confined Dewetting. *Langmuir* **2003**, *19*, 9714−9718.
(29) Yang, S. K.; Xu, F.; Ostendorp, S.; Wilde, G.; Zhao, H.; Lei, Y. Template-Confined Dewetting Process to Surface Nanopatterns: Fabrication, Structural Tunability, and Structure-Related Properties. *Adv. Funct. Mater.* **2011**, *21*, 2446−2455.
(30) Kim, B. H.; Lee, H. M.; Lee, J. H.; Son, S. W.; Jeong, S. J.; Lee, S.; Il Lee, D.; Kwak, S. U.; Jeong, H.; Shin, H.; Yoon, J. B.; Lavrentovich, O. D.; Kim, S. O. Spontaneous Lamellar Alignment in Thickness-Modulated Block Copolymer Films. *Adv. Funct. Mater.* **2009**, *19*, 2584−2591.
(31) Kim, B. H.; Shin, D. O.; Jeong, S. J.; Koo, C. M.; Jeon, S. C.; Hwang, W. J.; Lee, S.; Lee, M. G.; Kim, S. O. Hierarchical Self-assembly of Block Copolymers for Lithography-free Nanopatterning. *Adv. Mater.* **2008**, *20*, 2303−2307.
(32) Huang, J. X.; Kim, F.; Tao, A. R.; Connor, S.; Yang, P. D. Spontaneous Formation of Nanoparticle Stripe Patterns Through Dewetting. *Nat. Mater.* **2005**, *4*, 896−900.
(33) Roberts, N. A.; Fowlkes, J. D.; Mahady, K.; Afkhami, S.; Kondic, L.; Rack, P. D. Directed Assembly of One- and Two-Dimensional Nanoparticle Arrays from Pulsed Laser Induced Dewetting of Square Waveforms. *ACS Appl. Mater. Interfaces* **2013**, *5*, 4450−4456.
(34) Prodan, E.; Radloff, C.; Halas, N. J.; Nordlander, P. A Hybridization Model for the Plasmon Response of Complex Nanostructures. *Science* **2003**, *302*, 419−422.
(35) Wang, L.; Clavero, C.; Huba, Z.; Carroll, K. J.; Carpenter, E. E.; Gu, D. F.; Lukaszew, R. A. Plasmonics and Enhanced Magneto-Optics in Core-Shell Co-Ag Nanoparticles. *Nano Lett.* **2011**, *11*, 1237−1240.
(36) Armelles, G.; Cebollada, A.; Garcia-Martin, A.; Montero-Moreno, J. M.; Waleczek, M.; Nielsch, K. Magneto-optical Properties of Core Shell Magneto-plasmonic Au-$CoxFe_3$-xO_4 Nanowires. *Langmuir* **2012**, *28*, 9127−9130.
(37) Diez, J. A.; Kondic, L. On the Breakup of Fluid Films of Finite and Infinite Extent. *Phys. Fluids* **2007**, *19*, 072107.
(38) Kelly, K. L.; Coronado, E.; Zhao, L. L.; Schatz, G. C. The Optical Properties of Metal Nanoparticles: The Influence of Size, Shape, and Dielectric Environment. *J. Phys. Chem. B* **2003**, *107*, 668−677.
(39) Atwater, H. A.; Polman, A. Plasmonics for Improved Photovoltaic Devices. *Nat. Mater.* **2010**, *9*, 865−865.
(40) Hutter, E.; Fendler, J. H. Exploitation of Localized Surface Plasmon Resonance. *Adv. Mater.* **2004**, *16*, 1685−1706.
(41) Anker, J. N.; Hall, W. P.; Lyandres, O.; Shah, N. C.; Zhao, J.; Van Duyne, R. P. Biosensing with Plasmonic Nanosensors. *Nat. Mater.* **2008**, *7*, 442−453.
(42) Albella, P.; Garcia-Cueto, B.; Gonzalez, F.; Moreno, F.; Wu, P. C.; Kim, T. H.; Brown, A.; Yang, Y.; Everitt, H. O.; Videen, G. Shape Matters: Plasmonic Nanoparticle Shape Enhances Interaction with Dielectric Substrate. *Nano Lett.* **2011**, *11*, 3531−3537.
(43) Nerkararyan, S.; Nerkararyan, K.; Janunts, N.; Pertsch, T. Generation of Hankel-type Surface Plasmon Polaritons in the Vicinity of a Metallic Nanohole. *Phys. Rev. B* **2010**, *82*, 245405.
(44) Filter, R.; Qi, J.; Rockstuhl, C.; Lederer, F. Circular Optical Nanoantennas: an Analytical Theory. *Phys. Rev. B* **2012**, *85*, 125429.
(45) Nguyen, T. D.; Fuentes-Cabrera, M.; Fowlkes, J. D.; Diez, J. A.; Gonzalez, A. G.; Kondic, L.; Rack, P. D. Competition between

Collapse and Breakup in Nanometer-Sized Thin Rings Using Molecular Dynamics and Continuum Modeling. *Langmuir* **2012**, *28*, 13960−13967.
(46) Gonzalez, A. G.; Diez, J. A.; Wu, Y. Y.; Fowlkes, J. D.; Rack, P. D.; Kondic, L. Instability of Liquid Cu Films on a SiO_2 Substrate. *Langmuir* **2013**, *29*, 9378−9387.
(47) Palik, E. D. *Handbook of Optical Constants of Solids*; Academic Press: New York, 1998.